THE JOURNAL OF PHYSICAL CHEMISTRY B
A JOURNAL OF THE AMERICAN CHEMICAL SOCIETY

pubs.acs.org/JPCB
Article

Structural Dynamics by NMR in the Solid State: II. The MOMD Perspective of the Dynamic Structure of Metal–Organic Frameworks Comprising Several Mobile Components

Eva Meirovitch,* Zhichun Liang, Robert W. Schurko, Stephen J. Loeb, and Jack H. Freed*

Cite This: J. Phys. Chem. B 2022, 126, 2452–2465

Read Online

ACCESS | Metrics & More | Article Recommendations | Supporting Information

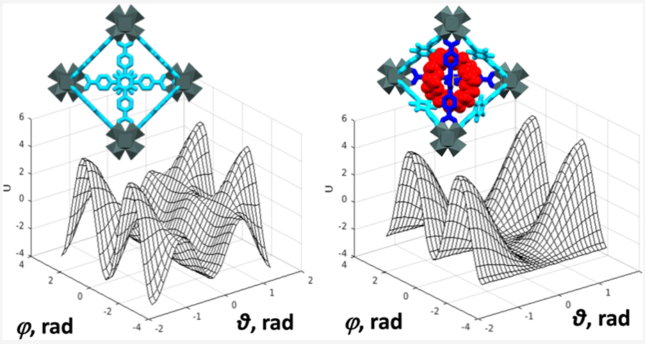

ABSTRACT: We describe the application of the microscopic-order-macroscopic-disorder (MOMD) approach, developed for the analysis of dynamic ^{2}H NMR lineshapes in the solid state, to unravel interactions among the constituents of metal–organic frameworks (MOFs) that comprise mobile components. MOMD was applied recently to University of Windsor Dynamic Material (UWDM) MOFs with one mobile crown ether per cavity. In this work, we study UWDM-9-d_4, which comprises a mobile ^{2}H-labeled phenyl-ring residue along with an isotopically unlabeled 24C8 crown ether. We also study UiO-68-d_4, which is structurally similar to UWDM-9-d_4 but lacks the crown ether. The physical picture consists of the NMR probe—the C–D bonds of the phenyl-d_4 rotor—diffusing locally (diffusion tensor $\boldsymbol{R}$) in the presence of a local ordering potential, u. For UiO-68-d_4, we find it sufficient to expand u in terms of four real Wigner functions, $D^L_{0|K|}$, overall 2–3 kT in magnitude, with $R_\parallel$ relatively fast, and $R_\perp$ in the (2.8–5.0) × 10^2 s^{-1} range. For UWDM-9-d_4, u requires only two terms 2–3 kT in magnitude and slower rate constants $R_\parallel$ and $R_\perp$. In the more crowded macrocycle-containing UWDM-9-d_4 cavity, phenyl-d_4 dynamics is more isotropic and is described by a simpler ordering potential. This is ascribed to cooperative phenyl-ring/macrocycle motion, which yields a dynamic structure more uniform in character. The experimental ^{2}H spectra used here were analyzed previously with a multi-simple-mode (MSM) approach where several independent simple motional modes are combined. Where possible, similar features have been identified and used to compare the two approaches.

1. INTRODUCTION

NMR lineshape analysis is a powerful method for studying internal molecular mobility in the solid state.[1−12] The carbon-bonded ^{2}H nucleus is a particularly useful probe. Invariably, the internal motion of the C–D bond is restricted spatially by its immediate molecular surroundings. There are three key elements characterizing restricted motions: the rates at which they occur (the kinetic component), the spatial restrictions they experience (the structural component), and associated features of local geometry (the geometric component).[9]

We have developed the microscopic-order-macroscopic-disorder (MOMD) approach[13] for the analysis of ^{2}H lineshapes from polycrystalline samples.[9,14−18] MOMD is based on the stochastic Liouville equation (SLE) developed by Freed and co-workers for generally treating restricted motions.[19−21] The three major elements mentioned above are treated for the entire motional range with due consideration to their three-dimensional tensorial properties.

The motion is expressed in MOMD by a diffusion tensor, $\boldsymbol{R}$. The spatial restrictions are represented by a local potential, u, expanded in the real Wigner functions, $D^L_{0|K|}$, which are closely related to the real spherical harmonics, Y_{LK}. The local geometry is given by the relative orientation of the MOMD-related $\boldsymbol{R}$ tensor frame and the NMR-related quadrupolar tensor frame, taken to be the same as the electric field gradient (EFG) tensor frame, as only C–D bonds and axially symmetric quadrupolar tensors are considered here. Model improvement is accomplished by enhancing the local potential and/or lowering the symmetry of the diffusion, ordering, and/or magnetic tensors. The potential, u, is an approximation to the potential of mean force (POMF) determined with molecular dynamics (MD) simulations.

MOMD has been applied so far to several different systems.[9,14−18] In all of these cases, MOMD spectra obtained with axial $\boldsymbol{R}$, u given by the terms D^2_{00} and $D^2_{0|2|}$, and the local geometry being largely standard in character, provided good fits to the experimental ^{2}H lineshapes. In a recent study,[18] we

Received: November 26, 2021
Revised: March 8, 2022
Published: March 25, 2022

https://doi.org/10.1021/acs.jpcb.1c10120

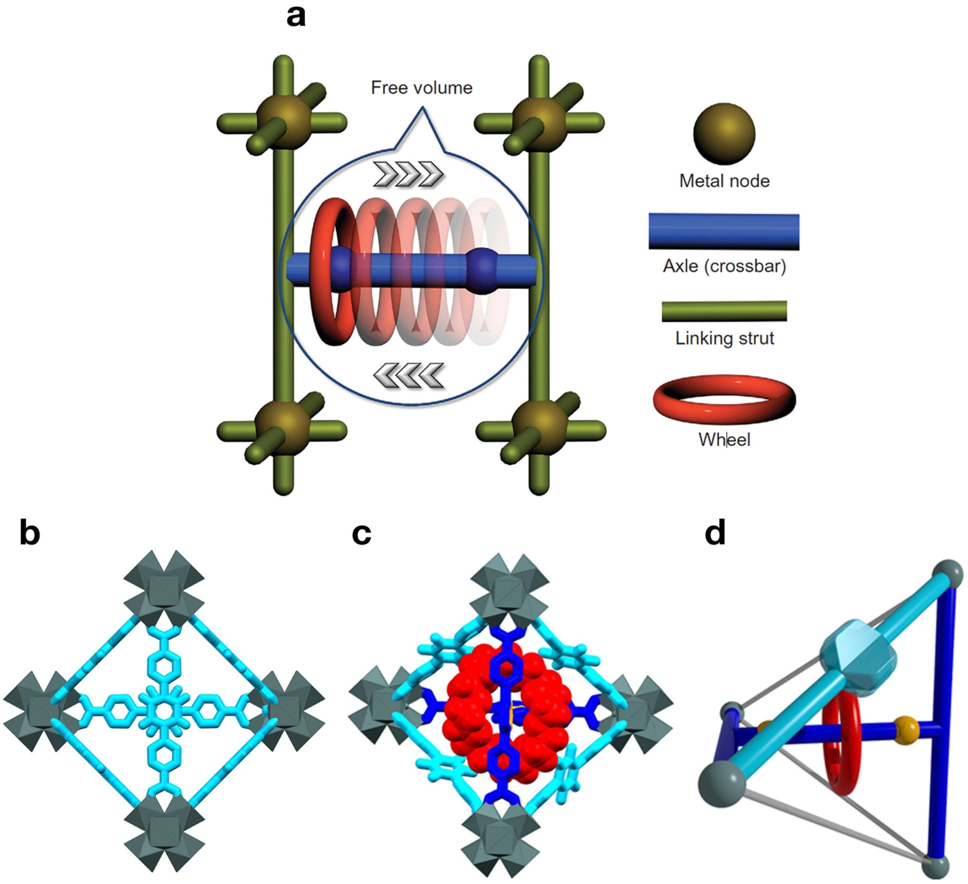

Figure 1. (a) Structural design of the basic UWDM MOF. (b) The tetrahedral cavity of UiO-68. (c) The tetrahedral cavity of UWDM-9-d_4 viewed down the [2]rotaxane crossbar showing the relative positions of the 24C8 macrocycle (red, space filling) and the central deuterated phenyl rotor of the primary linker TPDC-d_4 (cyan). (d) Super-tetrahedral cavity of UWDM-9-d_4 showing the relative positioning of the phenyl-d_4 rotor and the 24C8 macrocycle. Reprinted with permission from ref 28. Copyright 2021 Cell Press.

reported the application of MOMD to metal−organic frameworks (MOFs) which comprise mobile mechanically interlocked molecules (MIMs) prepared at the University of Windsor,[22−25] hence called University of Windsor Dynamic Materials (UWDMs). The mobile MIMs, consisting of crown-ether macrocycles, were ^{2}H-labeled.

The basic UWDM design is depicted in Figure 1a.[26] The MOF is made of linking struts (green) and metal nodes (brown), and the MIM consists of an axle (blue) and a mobile crown ether (i.e., a [2]rotaxane linker) (red wheel). In ref 18, several different UWDMs, comprising several different mobile ^{2}H-labeled crown ethers, were studied. The goal has been to identify common chemical and/or physical characteristics that might help in the rational design of MOF/MIM-based molecular machines. This requires consistent analysis of the systems to be compared by using appropriate selections of $\boldsymbol{R}$, u, and standard local geometry, as described above.

MOMD pointed to considerable differences between MIMs located in loose versus tight spaces; in the latter cases, changes in both the symmetry of the local potential and the coordination character of the deuterium-bonded carbon atom were detected.[18] Herein, we examine the effect of a ^{2}H-unlabeled crown ether on the restricted motion of a second mobile component, a ^{2}H-labeled phenyl-ring residue. The exceptionally stable MOF UiO-68-d_4 (Figure 1b)[27] and the MOF UWDM-9-d_4 are considered. UiO-68-d_4 comprises terphenyldicarboxylate (TPDC) as the primary linker, in which the central phenyl ring is mobile. The authors of ref 28 labeled this phenyl ring with deuterium, creating the "phenyl-d_4 rotor", on which we focus herein as a probe. UWDM-9-d_4 is structurally similar to UiO-68-d_4 except that it also comprises a [2]rotaxane linker with a mobile 24C8 crown ether (Figure 1c,d).[28] Thus, we are in a position to use MOMD to study the restricted motion of the mobile phenyl-d_4 ring both in the absence (UiO-68-d_4) and in the presence (UWDM-9-d_4) of the mobile crown ether. Figures 2a and 2b (ref 28) show the schematics of UiO-68-d_4 and UWDM-9-d_4, respectively, with the mobile components depicted.

^{2}H NMR spectra of UiO-68-d_4 and UWDM-9-d_4 acquired in ref 28 over the −100 to 175 °C temperature range are used as experimental data. The main objective is to quantify all of the key elements of the MOMD model: local potential, local diffusion tensor, and relevant features of local geometry. Of particular interest are differences between the internal motions of the phenyl-d_4 rotor with and without the macrocycle. We aim at determining the form of the POMF, u, and of the associated equilibrium probability distribution for bond vector orientation, $\exp(-u)$, at typical C−D sites. Features not set as objectives at the start but rather revealed over the course of this study include local structural changes in UiO-68-d_4. Likewise, our results point to cooperative motion of the two dynamic components of UWDM-9-d_4.

The same experimental data were analyzed in ref 28 with a different method, which we call the multi-simple-mode

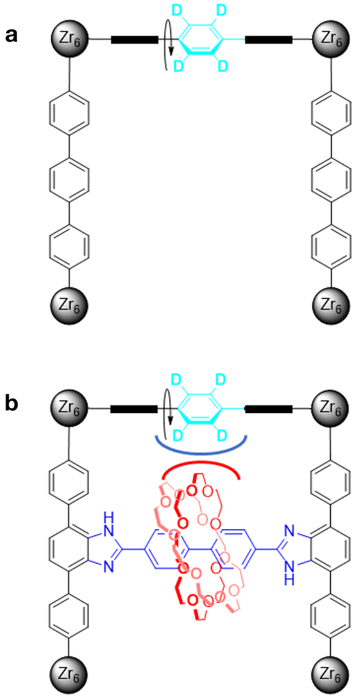

Figure 2. (a) Schematic showing the mobile phenyl-d_4 ring in the UiO-68-d_4 cavity. (b) Schematic showing the mobile phenyl-d_4 ring and the mobile 24C8 macrocycle in the UWDM-9-d_4 cavity. Reprinted with permission from ref 28. Copyright 2021 Cell Press.

(MSM) approach.[9] There are no limitations to the number and character of the simple (noncollective) motional modes employed. Typically, different overall models are used for different systems and often for different temperatures associated with a given system.

The MOMD theory is summarized briefly in Section 2. Section 3 is devoted to the results and discussion. Our conclusions appear in Section 4.

2. THEORETICAL BACKGROUND

The MOMD theory as applied to ^{2}H NMR has been described previously.[9,14−18] For convenience, its basics are outlined below. Figure 3a shows the MOMD frame scheme for the deuterium nucleus involved in restricted local motion. L is the space-fixed laboratory frame, and C is the local director frame fixed in the molecule, given in this case by the equilibrium orientation of the C−D bond. M denotes the principal axis system (PAS) of the local ordering tensor, **S**, defined in terms of the restricting/ordering potential, *u*. For simplicity, the PAS of the local ordering tensor and the PAS of the local diffusion tensor, ***R***, are taken as the same. Q denotes the PAS of the quadrupolar tensor. The M and Q frames are fixed in the probe, in this case the C−D bond attached rigidly to the phenyl-d_4 ring.

The Euler angles Ω_{CM} are time-dependent due to the molecular motions. The Euler angles $\Omega_{MQ} = (\alpha_{MQ}, \beta_{MQ}, \gamma_{MQ})$ are time-independent. Given that here the Q frame is axially symmetric, as our NMR probe is the C−D bond, one has $\gamma_{MQ} = 0$. For convenience, the angle α_{MQ} is set equal to zero. Thus, the orientation of Z_M (main ordering/diffusion axis) relative to Z_Q (the principal axis of the quadrupolar tensor pointing along the C−D bond) is given by the polar angle, β_{MQ}, called the "diffusion tilt" angle.[20]

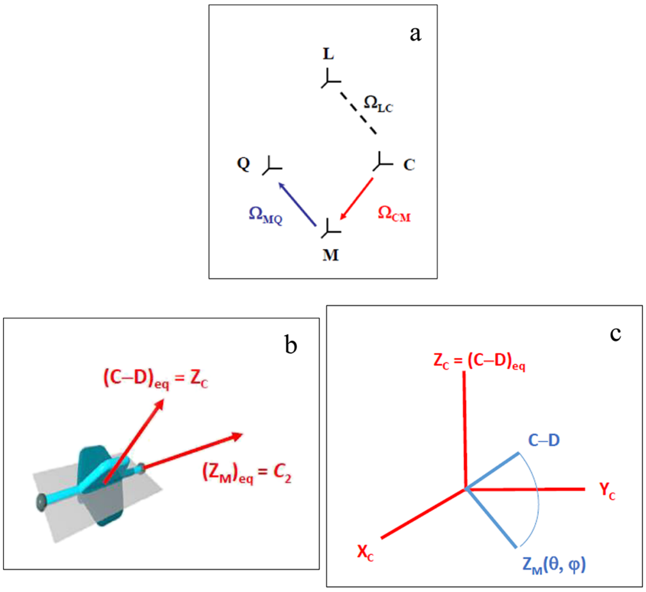

Figure 3. (a) MOMD frame structure. L, space-fixed laboratory frame; C, molecule-fixed local director frame; M, probe-fixed ordering/diffusion frame; Q, probe-fixed quadrupolar frame. The Euler angles Ω_{CM} are time-dependent due to molecular motion, the Euler angles Ω_{MQ} are time-independent, and the Euler angles Ω_{LC} are distributed in space at random. The arrows relate to the dynamical model and the dashed lines to the sample morphology. (b) The four stable states among which the phenyl-d_4 ring of UiO-68-d_4 exchanges in MSM, with "C_2" denoting the longitudinal pseudo-C_2 axis of this ring (represented by the moiety colored in cyan). The pseudo-C_2 axis in MSM is (approximately) the formal analogue of $(Z_M)_{eq}$ in MOMD. The transverse symmetry axis of the phenyl-d_4 ring is (approximately) the equilibrium/average C−D orientation, $(C{-}D)_{eq}$, in both MOMD and MSM. (c) Orientation of the main diffusion/ordering axis, Z_M, in the director frame, C.

The stochastic Liouville equation (SLE) for a particle diffusing in an anisotropic medium, for the special case where the director is parallel to the applied magnetic field ($\Omega_{LC} = 0$), is given by[19]

$$\left(\frac{\partial}{\partial t}\right)\rho(\Omega, t) = [-i\mathcal{H}(\Omega)^{X} - \Gamma_{\Omega}]\,\rho(\Omega, t), \text{ with } \Gamma_{\Omega}P_0(\Omega) = 0 \qquad (1)$$

The Euler angles $\Omega \to (\alpha, \beta, \gamma)$ are the same as Ω_{CM} in the notation above. Γ_Ω is a Markovian operator for the rotational reorientation of the spin-bearing moiety (the physical probe, in this case the C−D bond). $\mathcal{H}(\Omega)^X$ is the quantum Liouville operator, i.e., the commutator superoperator defined in terms of $\mathcal{H}(\Omega)$, the probe spin Hamiltonian describing the magnetic interactions. $P(\Omega, t)$ is the probability of finding Ω at the particular state at time, *t*, and $P_0(\Omega)$ is the unique equilibrium probability distribution of $P(\Omega, t)$ defined by $\Gamma_\Omega P(\Omega, t) = 0$. $\rho(\Omega, t)$ is the density matrix operator describing the joint evolution of the quantum spin degrees of freedom and the classical motion coordinates, Ω.

A simple form of the diffusion operator, Γ_Ω, is[19]

$$-\Gamma_{\Omega} = R\nabla^2_{\Omega}P(\Omega, t) - (R/kT)(\sin\beta)^{-1}\partial/\partial\beta[\sin\beta\,\mathbf{T}P(\Omega, t)] \qquad (2)$$

where *R* is the isotropic rotational diffusion rate, ∇^2_Ω is the rotational diffusion operator in the Euler angles, Ω, and **T** is

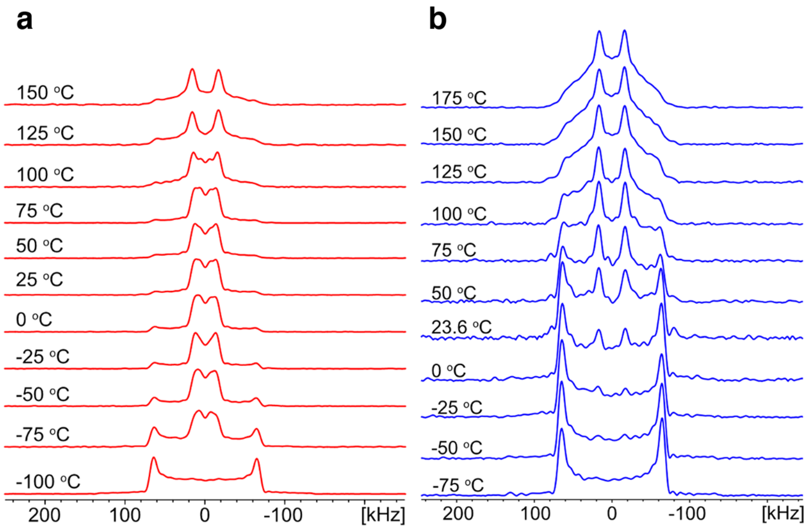

Figure 4. (a) Experimental ^{2}H NMR spectra of UiO-68-d_4 as a function of temperature.(b) Experimental ^{2}H NMR spectra of UWDM-9-d_4 as a function of temperature. Reprinted with permission from ref 28. Copyright 2021 Cell Press.

the restoring torque. The latter is equal to $\partial u/\partial\beta$ for an axial restoring potential, e.g., $u \cong -3/2\ c_0^2 \cos^2\beta$ (u is given in units of kT; i.e., it is dimensionless). The expression of Γ_Ω for rhombic diffusion tensor and rhombic potential is given in ref 20. Reference 21 comprises the extension of the theory to arbitrary Ω_{LC}.

In polycrystalline morphologies discussed herein, there is no "macroscopic order" aligning the molecules. Therefore, one has to calculate ^{2}H NMR spectra for a large enough number of director orientations (i.e., Ω_{LC} values) and sum the individual lineshapes according to random distribution; this completes the MOMD model.[9,13]

In this study, we are using an axial diffusion tensor, $\boldsymbol{R}$, associated in the absence of a restricting potential with three decay rates, $\tau_K^{-1} = 6R_\perp + K^2(R_\parallel - R_\perp)$,where $K = 0, 1, 2$ (K is the order of the rank-2 diffusion tensor). $R_\parallel$ and $R_\perp$ are the principal values of $\boldsymbol{R}$; one may also choose to define $\tau_\parallel = 1/(6R_\parallel)$ and $\tau_\perp = 1/(6R_\perp)$.[20]

For a uniaxial local director, one may expand the potential in the complete basis set of the Wigner rotation matrix elements with $M = 0$, $D_{0,K}^L(\Omega_{CM})$. One has[19−21]

$$u(\Omega_{CM}) = \frac{U(\Omega_{CM})}{kT} = -\sum_{L=1}^{\infty}\sum_{K=-L}^{+L} c_K^L D_{0,K}^L(\Omega_{CM}) \tag{3}$$

with c_K^L being dimensionless. If only the lowest $L = 2$ terms are kept, one obtains the real potential:[20,21]

$$u(\Omega_{CM}) = -c_0^2 D_{0,0}^2(\Omega_{CM}) - c_2^2[D_{0,2}^2(\Omega_{CM}) + D_{0,-2}^2(\Omega_{CM})] \tag{4}$$

Note that we did not consider the lowest $L = 1$ terms. They could be considered[29] but are typically omitted in view of the second-rank ($L = 2$) nature of the quadrupolar tensor.[30]

The order parameters for $L = 2$ are defined as[20]

$$\langle D_{0,K}^2(\Omega_{CM})\rangle = \int d\Omega_{CM} D_{0,K}^2(\Omega_{CM})\exp[-u(\Omega_{CM})]/\int d\Omega_{CM}\exp[-u(\Omega_{CM})],\ K = 0,\ 2 \tag{5}$$

For at least threefold symmetry around the local director, C, and at least twofold symmetry around the principal axis of the local ordering tensor, Z_M, only the irreducible tensor components $S_0^2 \equiv \langle D_{0,0}^2(\Omega_{CM})\rangle$ and $S_2^2 \equiv \langle D_{0,2}^2(\Omega_{CM}) + D_{0,-2}^2(\Omega_{CM})\rangle$ survive.[20] The Cartesian order parameters relate to S_0^2 and S_2^2 as $S_{xx} = (\sqrt{3/2}\,S_2^2 - S_0^2)/2$, $S_{yy} = -(\sqrt{3/2}\,S_2^2 + S_0^2)/2$, and $S_{zz} = S_0^2$.

In this study, the potential of eq 4 is enhanced to also comprise the $L = 4$, $K = 0$ and $L = 4$, $K = 2$ terms; the enhanced form is given by

$$u(\Omega_{CM}) = -c_0^2 D_{00}^2(\Omega_{CM}) - c_2^2 D_{0|2|}^2(\Omega_{CM}) - c_0^4 D_{00}^4(\Omega_{CM}) - c_2^4 D_{0|2|}^4(\Omega_{CM}) \tag{6}$$

The implementation of the MOMD approach in terms of an effective computer program is described in refs 13 and 31. Reference 31 is a user's guide for the calculation of slow-motional magnetic resonance spectra (here, ^{2}H spectra) for given values of Ω_{LC}. Reference 13 is the article where MOMD was originally described; the superposition of individual slow-motional (EPR) lineshapes according to random distribution of Ω_{LC} is discussed in some detail in that article.

To carry out a MOMD calculation, one has to specify the external magnetic field; the quadrupolar coupling constant, C_Q; the intrinsic linewidth, $(1/T_2{}^*)$; the number of Ω_{LC} values for which slow-motional lineshapes are to be calculated; and the technical parameters associated with the calculation of slow-motional (NMR or ESR) spectra.[31] The physical parameters to be specified and varied include, e.g., the coefficients c_0^2 and c_2^2 for the potential of eq 4 and the diffusion rate constants $R_\parallel$ and $R_\perp$. Typically, the "diffusion tilt", β_{MQ}, is fixed at its standard value, but when necessary, it is allowed to vary.

It is of interest to relate the MOMD frame structure of Figure 3a to the MSM framework to be able to compare the two approaches. This requires identifying common features in the respective approaches; an attempt to do so is illustrated in Figure 3. The item colored in cyan in Figure 3b illustrates the four-site-exchange mode that is one of the constituents of the overall MSM model for UiO-68-d_4 dynamics. For UWDM-9-d_4, this would be six-site exchange and different additional motional modes. The axis around which four- or six-site exchange takes place is the longitudinal symmetry axis of the

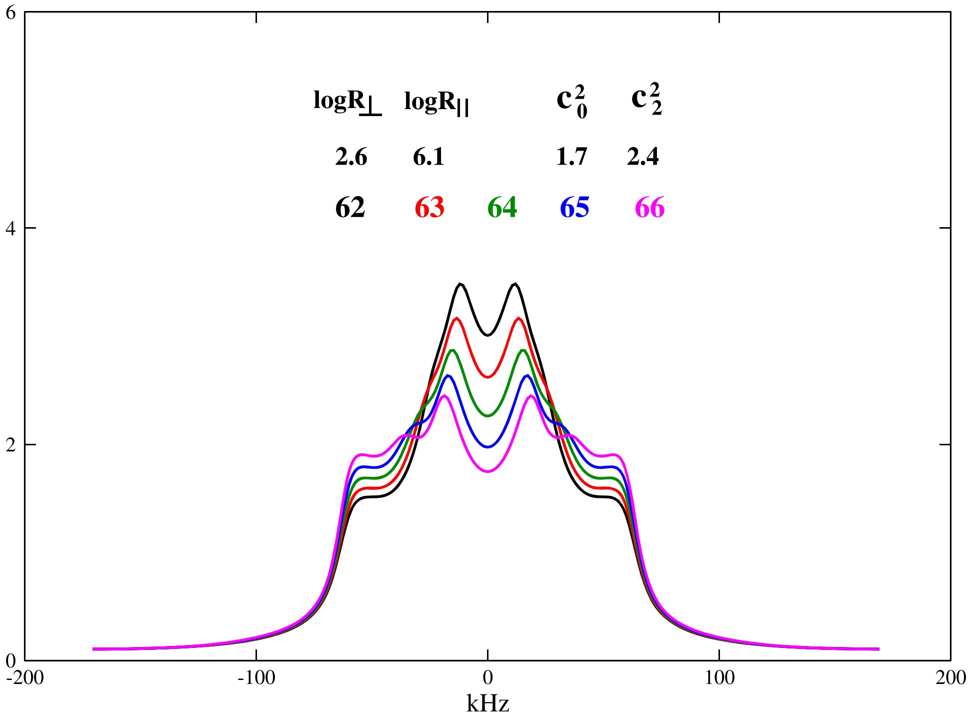

Figure 5. Simulated ^{2}H MOMD spectra for log $R_\perp$, log $R_\parallel$, c_0^2, and c_2^2 obtained with the diffusion tilt, β_{MQ}, in the 62−66° range. $R_\perp$ and $R_\parallel$ are given in units of s^{-1}, the quadrupolar coupling constant is C_Q = 180 kHz (η = 0), and the intrinsic linewidth is 1 kHz. This figure refers to both UiO-68-d_4 and UWDM-9-d_4.

phenyl-d_4 ring, called "pseudo-C_2 axis" in the MSM formalism.[28]

Let us ignore for the present the additional (different) sets of motional modes that contribute to the overall MSM models for UiO-68-d_4 and UWDM-9-d_4 dynamics. In this case, the pseudo-C_2 axis in MSM may be considered to be the formal analogue of $(Z_M)_{eq}$, the equilibrium orientation of the main ordering/diffusion axis, Z_M, in MOMD. "Equilibrium orientation" means in this context "most probable orientation", i.e., the orientation where the corresponding POMF has minimum value. In addition to this analogy, all of the vector quantities in both MOMD and MSM are defined with respect to the equilibrium/average orientation of the C−D bond, $(C-D)_{eq}$, which is the Z axis of the local director frame, C, in Figure 3a. Within a reasonably good approximation, $(C-D)_{eq}$ is pointing along the transverse symmetry axis of the phenyl-d_4 ring.

The POMFs (related to spherical harmonics) are given in spherical coordinates, θ and φ; the probability distributions are given (for convenience and simple insight[32]) in Cartesian coordinates. θ and φ define the orientation of the main ordering/diffusion axis, Z_M, in the director frame; this is illustrated in Figure 3c. As specified above, $(Z_M)_{eq}$ and $(C-D)_{eq}$ are approximately perpendicular to one another in the C-frame; so are Z_M and C−D in the M-frame (Figure 3c).

3. RESULTS AND DISCUSSION

3.1. Qualitative Description of the Experimental Spectra.

3.1.1. The UiO-68-d_4 System. Figure 4a shows the experimental ^{2}H spectra of UiO-68-d_4 as a function of temperature.[28] At −100 °C, the rigid-limit (RL) spectrum is observed, with the perpendicular divergences separated by approximately 128 kHz (ideally, this parameter is 180 × 3/4 = 135 kHz). At −75 °C, an abrupt change in the ^{2}H spectrum occurs: the perpendicular divergences are preserved with reduced intensity, and a new pair of inner divergences with an unusual rounded-peak appearance, separated by approximately 27 kHz, emerges.[28] Except for a decrease in the intensity of the outer (perpendicular) divergences, the ^{2}H spectrum changes to a small extent up to 75 °C. Then it alters again considerably around 100 °C to the extent that, at 125 °C, the inner divergences assume the usual sharp-peak appearance, and their separation is augmented by approximately 12% (Figure 4a). Virtually no further change occurs above 125 °C until the sample starts to decompose above 200 °C.[28]

3.1.2. The UWDM-9-d_4 System. Figure 4b shows the experimental ^{2}H spectra of UWDM-9-d_4 as a function of temperature.[28] At −75 °C, the RL powder-pattern is observed, with the perpendicular divergences separated by approximately 128 kHz. At −50 °C, the weak inner pair of divergences separated by approximately 27 kHz, also seen for UiO-68-d_4 (Figure 4a), becomes visible. While the −75 °C spectrum of UiO-68-d_4 is very different from the RL spectrum, the −50 °C spectrum of UWDM-9-d_4 was found to evolve gradually from the RL spectrum. In the −50 to 75 °C range, the intensity ratio between the inner and outer divergences increases, with the separation of the outer divergences decreasing somewhat. Around 75 °C, intensity starts building up in the region between the inner and outer divergences. This process continues beyond 125 °C.

3.2. Relevant Parameter Ranges.

The local diffusion tensor, $\boldsymbol{R}$, is taken as axially symmetric; its principal values are $R_\parallel$ and $R_\perp$ (in s^{-1}), reported in many cases as log $R_\parallel$ and log $R_\perp$. On the logarithmic scale, the dynamic window extends from 2.1 to 6.2.

As discussed above, the local potential, u, is expanded in the basis set of the Wigner functions, which are the real combinations, $D_{0|K|}^L = [D_{0-K}^L + (-1)^K D_{0K}^L]$, of the Wigner rotation matrix elements, D_{MK}^L, with $M = 0$. This expansion has

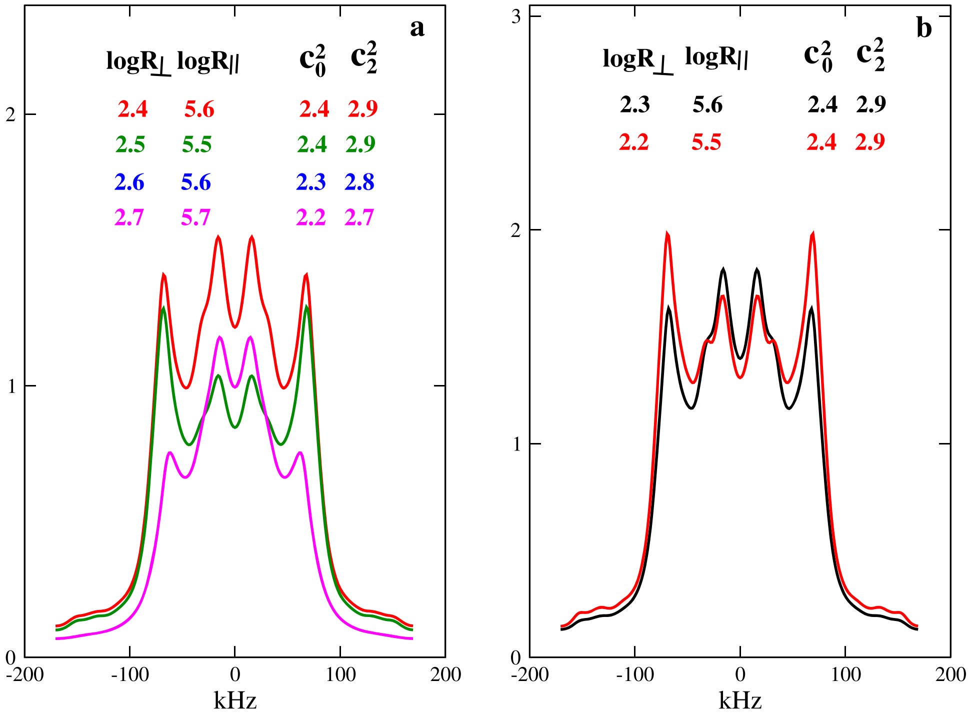

Figure 6. Simulated ^{2}H MOMD spectra for log $R_\perp$, log $R_\parallel$, c_0^2, and c_2^2 referring to UWDM-9-d_4. Other parameters are as described in the caption of Figure 5.

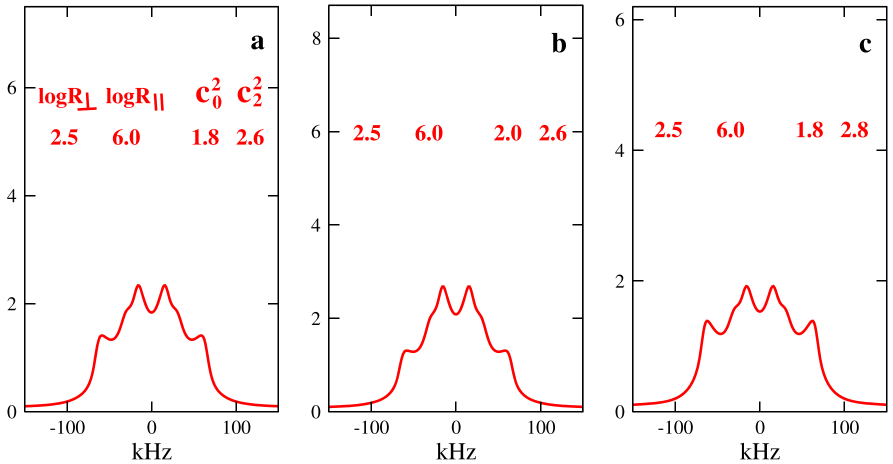

Figure 7. Simulated ^{2}H MOMD spectra for log $R_\perp$, log $R_\parallel$, c_0^2, and c_2^2 referring to UiO-68-d_4. Other parameters are as described in the caption of Figure 5.

to be truncated prior to applying MOMD to actual experimental spectra. The lowest-even-*L* axial potential is $u = -c_0^2 D_{00}^2$, and the lowest-even-*L* rhombic potential is $u = -c_0^2 D_{00}^2 - c_2^2 D_{0|K|}^2$ (eq 4). Adding the next terms of the expansion, D_{00}^4 and $D_{0|2|}^4$, yields the potential $u = -c_0^2 D_{00}^2 - c_2^2 D_{0|2|}^2 - c_0^4 D_{00}^4 - c_2^4 D_{0|2|}^4$ (eq 6). Thus far we found that the local potential at the site of the motion of methyl and phenyl moieties in proteins is weak.[9,13−18]

The Euler angles $\Omega_{MQ} = (\alpha_{MQ}, \beta_{MQ}, \gamma_{MQ})$ underlie the transformation from M, the PAS of the local diffusion/local ordering tensor, to Q, the PAS of the quadrupolar tensor. As pointed out in the theoretical background (Section 2), $\alpha_{MQ} = \gamma_{MQ} = 0°$. The diffusion tilt, β_{MQ}, specifies the orientation of the main local diffusion/local ordering axis with respect to the C−D bond. Schadt et al.[33] have shown that diffusion with $\beta_{MQ} = 64°$ is the diffusive-motion analogue of the π-flip model for benzene and phenyl moieties. Thus, the value of $\beta_{MQ} \sim 64°$, potential coefficients of 2−3 *kT*, and diffusion rate constants in the 2−6 range on a logarithmic scale are considered. Extensive MOMD simulations were performed to narrow the parameter ranges of the diffusion rate constants: log $R_\perp$ is expected to reside in the 2.3−2.9 range; and log $R_\parallel$, in the 5.5−6.2 range.

Figure 5 illustrates the effect of the diffusion tilt angle, β_{MQ}, in the vicinity of 64° for typical values of c_0^2, c_2^2, $R_\parallel$, and $R_\perp$. Diffusion tilt values in the 62−66° range can yield, together with appropriate potential coefficients and diffusion rate constants, experimental divergence separations of *ca.* 128 kHz and *ca.* 27 kHz for the outer and inner peaks, respectively.

Keeping β_{MQ} fixed at 64°, we show in Figure 6 the ^{2}H spectra for log $R_\perp$ in the 2.2−2.7 range, log $R_\parallel$ in the 5.5−5.7 range, c_0^2 in the 2.2−2.4 range, and c_2^2 in the 2.7−2.9 range. These are the parameter ranges where the separations between

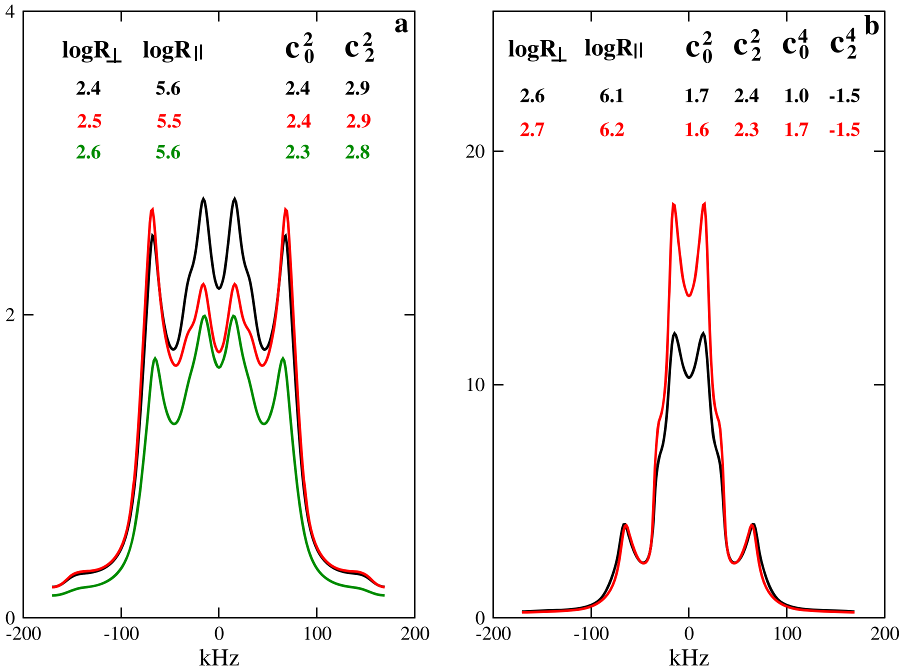

Figure 8. (a) Simulated ^{2}H MOMD spectra for log $R_\perp$, log $R_\parallel$, c_0^2, and c_2^2 assessing the parameter ranges appropriate for UWDM-9-d_4. (b) Simulated ^{2}H MOMD spectra for log $R_\perp$, log $R_\parallel$, c_0^2, c_2^2, c_0^4, and c_2^4 assessing the parameter ranges appropriate for UiO-68-d_4. Other parameters are as described in the caption of Figure 5.

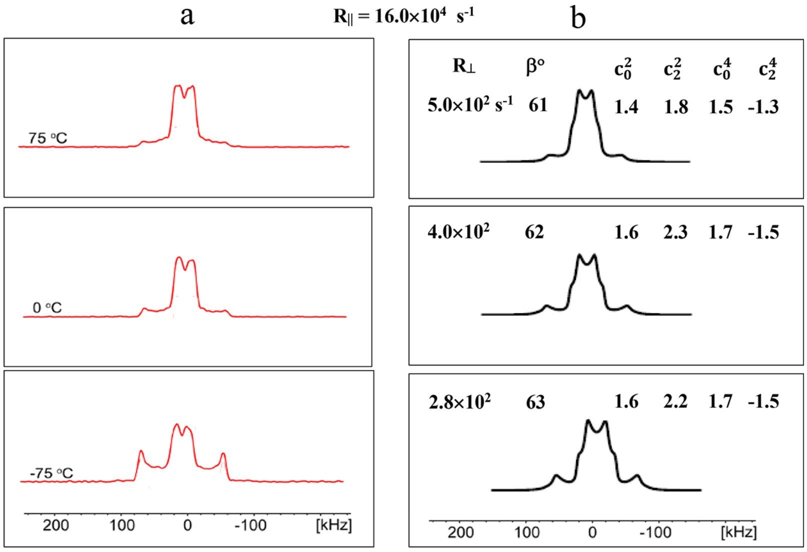

Figure 9. (a) Experimental UiO-68-d_4 spectra acquired at −75, 0, and 75 °C (*cf.* Figure 4a). (b) Best-fit calculated MOMD spectra obtained using the parameters depicted in the figure and given in Table 1 (*cf.* main text for details). The error in the polar angle, β_{MQ}, is ±1.5%; the error in the potential coefficients is ±5%; and the error in the diffusion rate constants is ±10%.[18] Reprinted with permission from ref 28. Copyright 2021 Cell Press.

the inner and outer divergences match well with experiment. The main difference among the Figure 6 spectra is a change in the relative intensities of the two divergence pairs (in ref 28, this feature is considered to represent for UWDM-9-d_4 a change in the relative weight of two superposed temperature-invariant spectral components).

Figure 7 shows efforts to reproduce the UiO-68-d_4 lineshapes, which represent phenyl-d_4 dynamics in the absence of the macrocycle. The traditional potential $u = -c_0^2 D_0^2 - c_2^2 D_{0|2|}^2$ was used. The diffusion rate constants, $R_\perp$ and $R_\parallel$, and the potential coefficients, c_0^2 and c_2^2, were varied within the parameter ranges determined above, even exceeding them. Although the inner and outer divergence separations were largely preserved, the overall shapes of the ^{2}H lineshapes were poorly reproduced. They could be improved considerably using $u = -c_0^2 D_{00}^2 - c_2^2 D_{0|2|}^2 - c_0^4 D_{00}^4 - c_2^4 D_{0|2|}^4$ instead of $u = -c_0^2 D_{00}^2 - c_2^2 D_{0|2|}^2$ (*cf.* Figure 8). Within the scope of reproducing major trends, UWDM-9-d_4 does not require the more elaborate potential form.

Figure 8a,b suggests parameter ranges wherein the best-fit parameters are to be sought for UiO-68-d_4 (*cf.* the region extending from −50 to 50 °C in Figure 4a) and for UWDM-9-d_4 (*cf.* the region extending from −25 to 50 °C in Figure 4b).

3.3. Analysis of the Experimental ^{2}H Spectra. MOMD is a more phenomenological approach that describes the structural dynamics in terms of an effective/collective mode. The MOMD parameters are inherently effective in their nature. Let us expand on this feature focusing on β_{MQ}, the angle between the diffusion axis for phenyl-ring motion and the C−D bond, to be determined in this section. For a diffusion axis pointing along the C_2 symmetry axis of the phenyl ring, one has $\beta_{MQ} = 64°$ (ref 33) and $\xi = 60°$, where ξ is the angle between C−D and C_2; we call this "standard local geometry" (see above). For an effective diffusion axis not pointing along C_2, one has $\beta_{MQ} \neq 64°$ and $\xi = 60°$; we call this "digression from standard local geometry". Average (i.e., effective) jump axes are used routinely in MSM models.[22−24]

The NMR lineshapes analyzed in this section quantitatively are inherently complex, requiring a detailed set of adjustable MOMD parameters for precise reproduction. Such a set could be created by lowering tensor symmetries and adding terms to the local potential. However, insightful comparison among sites and instances, including comparison between MOMD and MSM, would be difficult because many different parameters are involved. Given that comparison is important here, we opted for limited and consistent sets of adjustable MOMD parameters. These sets reproduce the main spectral features and exhibit physically relevant temperature dependence of the various parameters. As shown below, with this approach similar characteristics could be identified for MOMD and MSM and used to compare the two approaches.

The experimental and calculated MOMD spectra are displayed similar to the manner in which the experimental and calculated MSM spectra are displayed in ref 28, i.e., side-by-side. To make possible assessing more conveniently the quality of the MOMD fits, we show in Figure S1 for UiO-68-d_4 and in Figure S2 for UWDM-9-d_4 corresponding experimental and calculated spectra aligned vertically, with the inner and outer divergences marked.

3.3.1. UiO-68-d_4. At −75 °C (Figure 4a), the ^{2}H spectrum changes abruptly.[28] This is interpreted as a local structural change that results in the onset of different symmetry of one or more parameters and/or the sudden emerging of new features of the dynamic structure. Increasing the temperature from −75 to 75 °C has a limited effect on the dynamic ^{2}H powder pattern, except for the outer divergences losing intensity in comparison with the inner divergences. We have selected for detailed analysis the spectra acquired at −75, 0, and 75 °C (Figure 9a).

The smallest set of parameters that reproduces the features delineated above is as follows. Based on Figures 5−8, the four-term potential $u = -c_0^2 D_{00}^2 - c_2^2 D_{0|2|}^2 - c_0^4 D_{00}^4 - c_2^4 D_{0|2|}^4$ is used (*cf.* Figure 9b). At −75 °C, we find that $c_0^2 = 1.6$, $c_2^2 = 2.3$, $c_0^4 = 1.7$, and $c_2^4 = -1.5$ are the best-fit potential coefficients, and $R_\perp = 2.8 \times 10^2$ s^{-1} and $R_\parallel = 1.0 \times 10^6$ s^{-1} are the best-fit diffusion rate constants (*cf.* Table 1). The standard value of β_{MQ}, associated in this case with diffusive motion of the phenyl-d_4 ring around the pseudo-C_2 axis, is 64°.[33] At −75 °C, the best-fit value of β_{MQ} is 63° (within the scope of data fitting, the difference from 64° is significant). At higher temperatures, β_{MQ} is smaller, gradually decreasing to 61° at 75 °C. In general, the potential coefficients decrease in proceeding from −75 to 75 °C, indicating that, in this temperature range, both the magnitude and the rhombicity of the potential decrease with increasing temperature. The parallel diffusion rate constant, $R_\parallel$, is already in the extreme motional narrowing limit at −75 °C, so no change can be observed with increasing temperature. The perpendicular diffusion rate constant, $R_\perp$, increases from 2.8×10^2 s^{-1} at −75 °C to 5.0×10^2 s^{-1} at 75 °C.

Table 1. Best-Fit MOMD Parameters Reproducing the Experimental ^{2}H Spectra of UiO-68-d_4 Acquired at −75, 0, 75, and 125 °C (Figures 4a, 9, and 10)

	$R_\perp$, s^{-1}	$R_\parallel$, s^{-1}	c_0^2	c_2^2	c_0^4	c_2^4	β_{MQ}°
125 °C	4.0×10^2	1.6×10^6	3.0	3.0	0.0	0.0	66
75	5.0×10^2	1.6×10^6	1.4	1.8	1.5	−1.3	61
0	4.0×10^2	1.6×10^6	1.6	2.3	1.7	−1.5	62
−75	2.8×10^2	1.6×10^6	1.6	2.3	1.7	−1.5	63

The outer (perpendicular) divergences in the experimental −75 °C spectrum are more intense than those in the corresponding MOMD spectrum. This experimental lineshape was also challenging for the MSM approach,[28] which to reproduce it considered three different exchange processes with rate constants on the order of 10^3−10^4 s^{-1}. Nevertheless, the central parts of experiment and simulation do not agree well (*cf.* Figure 3A of ref 28). MOMD adequately reproduces the central part of the experimental −75 °C spectrum but encounters difficulties with the outer divergences (Figure 9). In ref 28, it was suggested that additional motional modes are most likely present, generally with minor spectral effect but with noticeable effect for some features.

As pointed out in Section 3.1, a sudden change in the ^{2}H lineshape of UiO-68-d_4 occurs around 100 °C (*cf.* Figure 4a). This is ascribed to yet another local structural change, or the emergence of a new feature of the dynamics, also found by MSM.[28] Quantitative reproduction of the experimental 125 °C lineshape (and the 150 °C lineshape, which is virtually the same) required a change in the polar angle, β_{MQ}, and in the form and strength of the potential, u. Figure 10a shows that $\beta_{MQ} = 66°$ is appropriate, and Figure 10b shows that the $L = 2$, $|K| = 0, 2$ potential suffices. We offer the black trace in Figure 10b as a reasonable calculated counterpart of the experimental 125 °C spectrum (Figure 4a). Detailed analysis will have to await the acquisition of additional experimental ^{2}H spectra in the 100−125 °C temperature range.

The best-fit MOMD parameters for the representative experimental UiO-68-d_4 spectra chosen for analysis are given in Table 1.

A future prospect is to combine mesoscopic MOMD with atomistic MD simulations to determine POMFs in proteins. Once this is available, better reproduction of the experimental ^{2}H spectra in Figure 9a might be achievable. Note that our current MOMD simulations do reproduce the unusual rounded-peak appearance of the inner divergences. The MSM analysis accounts for the key discontinuities at all temperatures, including the increased spacing between the inner discontinuities with increasing temperature. However, the shape of the inner divergences could not be well reproduced; it was ascribed to residual signals arising from intermediate motional regime motions and/or distributions of motional rates.[28,34] The quality of the fit can be conveniently assessed by inspecting Figure S1 of the Supporting Information.

3.3.2. UWDM-9-d_4. The representative experimental ^{2}H spectra acquired at 0, 50, and 125 °C shown in Figure 11a have been selected for analysis. The best-fit MOMD spectra are

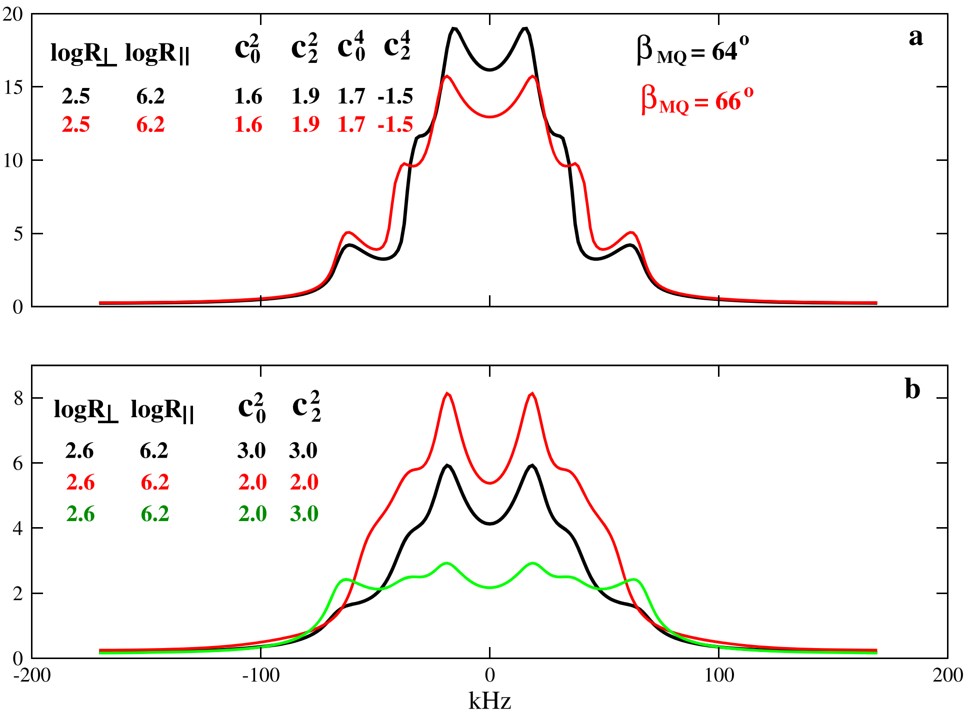

Figure 10. Simulated MOMD spectra referring to the experimental spectrum of UiO-68-d_4 acquired at 125 °C. (a) Log $R_\perp$, log $R_\parallel$, c_0^2, c_2^2, c_0^4, and c_2^4, as depicted in the figure; β_{MQ} = 64° (black) and β_{MQ} = 66° (red). (b) Log $R_\perp$, log $R_\parallel$, c_0^2, and c_2^2, as depicted in the figure; β_{MQ} = 66°. Other parameters are as described in the caption of Figure 5.

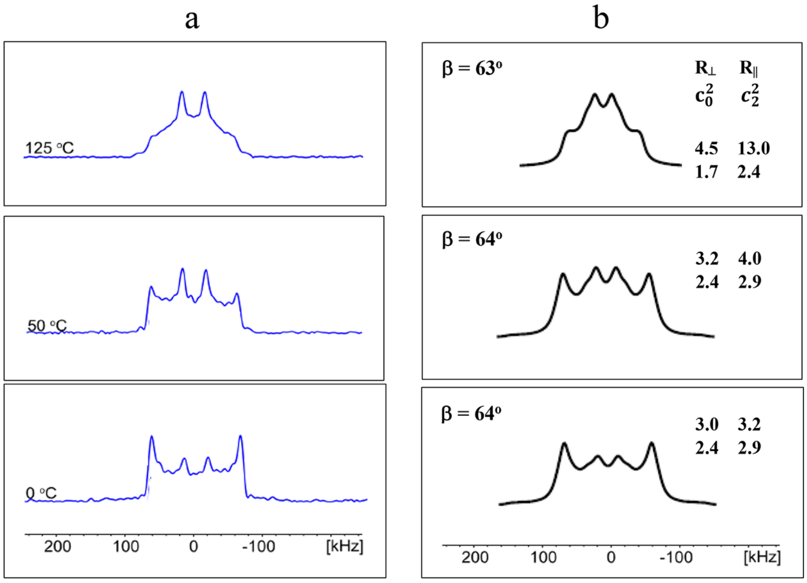

Figure 11. (a) Experimental UWDM-9-d_4 spectra acquired at 0, 50, and 125 °C (*cf.* Figure 4b). (b) Best-fit calculated MOMD spectra obtained using the parameters depicted in the figure and given in Table 2. The diffusion rate constants, $R_\perp$ and $R_\parallel$, are given in units of 10^2 and 10^4 s^{-1}, respectively. Error estimates are as described in the caption of Figure 9. Reprinted with permission from ref 28. Copyright 2021 Cell Press.

shown in Figure 11b. The potential $u = -c_0^2 D_{00}^2 - c_2^2 D_{0|2|}^2$ suffices for reproducing the main features of the experimental spectra. All four parameters, c_0^2, c_2^2, $R_\perp$, and $R_\parallel$, change as a function of temperature. β_{MQ} is equal to 64° at 0 and 50 °C and to 63° at 125 °C. In the 0 to 125 °C range, $R_\perp$ increases from 3.0×10^2 to 4.5×10^2 s^{-1} and $R_\parallel$ from 3.2×10^5 to 1.3×10^6 s^{-1}; c_0^2 decreases from 2.4 to 1.7 and c_2^2 from 2.9 to 2.4 (Table 2). The quality of the fit can be conveniently assessed by inspecting Figure S2 of the Supporting Information.

Table 2. Best-Fit MOMD Parameters Reproducing the Experimental ^{2}H Spectra of UWDM-9-d_4 Acquired at 0, 50, and 125 °C (Figure 11)

	$R_\perp$, s^{-1}	$R_\parallel$, s^{-1}	c_0^2	c_2^2	β_{MQ}°
125 °C	4.5×10^2	1.3×10^6	1.7	2.4	63
50	3.2×10^2	4.0×10^5	2.4	2.9	64
0	3.0×10^2	3.2×10^5	2.4	2.9	64

https://doi.org/10.1021/acs.jpcb.1c10120
J. Phys. Chem. B 2022, 126, 2452−2465

Table 3. Best-Fit MOMD Parameters Reproducing the ^{2}H Spectra of UiO-68-d_4 and UWDM-9-d_4 Acquired at 0 °C

	$R_\perp$, s^{-1}	$R_\parallel$, s^{-1}	c_0^2	c_2^2	c_0^4	c_2^4	β_{MQ}°
0 °C UiO-68	4.0×10^2	1.6×10^6	1.6	2.3	1.7	−1.5	62
0 °C UWDM-9	3.0×10^2	3.2×10^5	2.4	2.9	NA	NA	64

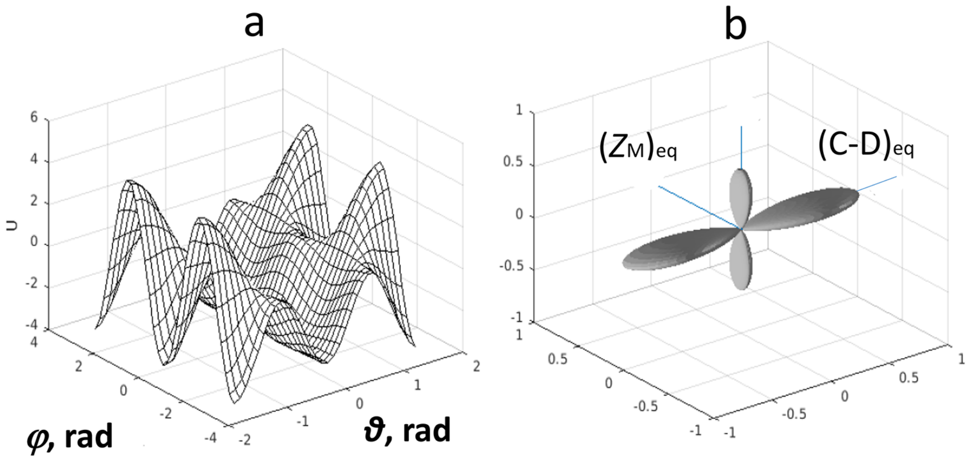

Figure 12. Typical (a) MOMD potential, *u*, given by eq 6, and (b) equilibrium probability distribution, $P_{eq} = \exp(-u)$, both depicted in the director frame, C (*cf.* Figure 3c). *u* is given in spherical coordinates and P_{eq} in Cartesian coordinates. These are best-fit functions corresponding to the experimental 0 °C ^{2}H spectrum of UiO-68-d_4. The equilibrium orientations of the main ordering/diffusion axis, $(Z_M)_{eq}$, and the C−D bond, $(C{-}D)_{eq}$, are specified in panel b.

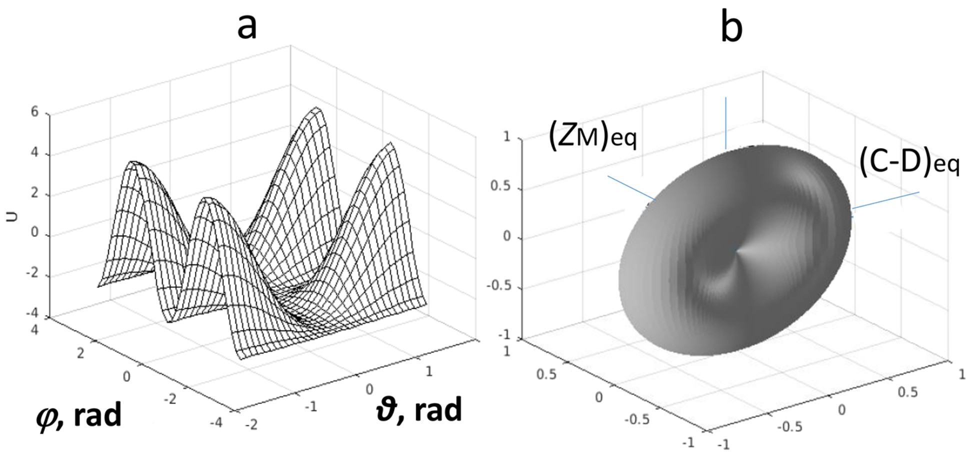

Figure 13. Typical (a) MOMD potential, *u*, given by eq 4, and (b) equilibrium probability distribution, $P_{eq} = \exp(-u)$, both depicted in the director frame, C (*cf.* Figure 3c). *u* is given in spherical coordinates and P_{eq} in Cartesian coordinates. These are best-fit functions corresponding to the experimental 0 °C ^{2}H spectrum of UWDM-9-d_4. The equilibrium orientations of the main ordering/diffusion axis, $(Z_M)_{eq}$, and the C−D bond, $(C{-}D)_{eq}$, are specified in panel b.

Table 4. Order Parameters Defined in Terms of the Potential Coefficients Given in Table 3

system	c_0^2	c_2^2	c_0^4	c_2^4	S_0^2	S_2^2	S_{xx}	S_{yy}	S_{zz}
UiO-68-d_4	1.6	2.3	1.7	−1.5	0.07	0.55	0.302	**−0.372**	0.07
UWDM-9-d_4	2.4	2.9	NA	NA	0.205	0.477	0.190	**−0.395**	0.205

The MOMD spectra in Figure 11b are not as resolved as their experimental counterparts in Figure 11a. They are also not as resolved in the MSM analysis, although in that study two contributing components were considered.[28] We ascribe this feature to fast local fluctuations.

3.4. Comparison between UiO-68-d_4 and UWDM-9-d_4.

For a detailed comparison, we focus on the 0 °C spectra. The set of UiO-68-d_4 spectra do not vary much with temperature; the 0 °C spectrum may be considered representative. A UWDM-9-d_4 spectrum acquired at the same temperature is available. Thus, the 0 °C pair may be considered to be typical for comparison. The pertinent best-fit MOMD parameters are shown in Table 3.

Figure 12a shows the best-fit MOMD potential that reproduces (together with the corresponding ***R***-tensor and β_{MQ} angle) the 0 °C ^{2}H spectrum of UiO-68-d_4. Figure 13a shows the analogous potential for UWDM-9-d_4. Both are given in spherical polar coordinates, (θ, φ), in the director frame (C frame in Figure 3a). The UiO-68-d_4 potential is given by eq 6 and the UWDM-9-d_4 potential by eq 4. Key features of these potentials will be discussed shortly.

One may define second-rank order parameters in terms of the coefficients of the MOMD potential either in irreducible tensor notation, S_0^2 and S_2^2, or in Cartesian tensor notation, S_{xx}, S_{yy}, and S_{zz}. The two sets relate to one another as $S_{xx} = (\sqrt{3/2}\,S_2^2 - S_0^2)/2$, $S_{yy} = -\left(\sqrt{\frac{3}{2}}\,S_2^2 + S_0^2\right)/2$, and $S_{zz} = S_0^2$ (*cf.* eqs 4 and 5 and section after eq 5). These quantities, calculated from the coefficients given in Table 3, are given in Table 4.

For both UiO-68-d_4 and UWDM-9-d_4, the Cartesian order parameter with the largest absolute value is S_{yy}, indicating that the main ordering axis (of the M frame in Figure 3a) is y (*cf.* Figure 3c). In both cases, S_{yy} is negative, indicating that y orients preferentially perpendicular to the local director. This situation is termed "perpendicular y-ordering". The data in Table 4 are consistent with the main local ordering axis being identified with the longitudinal symmetry axis of the phenyl-d_4 ring and the Z axis of the local director frame being identified with the equilibrium orientation of the C−D bond.

Figures 12b and 13b show the equilibrium probability distributions, $P_{eq} = \exp(-u)$, derived from the potentials illustrated in Figures 12a and 13a. They illustrate the spatial distribution of the main ordering axis, Z_M (hence also the probe, C−D; *cf.* Figure 3c) in the director frame, C. Cartesian coordinates ($x = \sin\theta\cos\varphi$, $y = \sin\theta\sin\varphi$, $z = \cos\theta$) are used in this representation.[32] The blue "lines" depict the most probable (equilibrium) M frames; the principal axes of these frames, $(Z_M)_{eq}$, are specified.

For UWDM-9-d_4, $S_{xx} \cong S_{zz}$, and both are positive. Accordingly, P_{eq} in Figure 13b is nearly disk-shaped. The corresponding POMF, shown in Figure 13a, has a minimum at $\varphi = \pm\pi/2$, in agreement with y ordering; it is nearly invariant along the θ coordinate, in agreement with nearly axial y ordering. For UiO-68-d_4, $S_{xx} \neq S_{zz}$, and both are positive. In accordance, P_{eq} in Figure 12b is asymmetric. The corresponding potential, shown in Figure 12a, has a minimum at $\varphi = \pm\pi/2$, in agreement with y ordering; it varies along the θ coordinate in a manner determined by the shape of the corresponding local potential.

The POMF of UWDM-9-d_4 is stronger (larger c_0^2), broader, and more symmetrical than the POMF of UiO-68-d_4 (*cf.* Figures 12a and 13a). The local motion of the phenyl-d_4 rotor is slower in UWDM-9-d_4 as compared to UiO-68-d_4 (Table 3). Stronger potential and slower motion in the presence of a mobile macrocycle may be ascribed to limited free volume. On the other hand, the POMF of UWDM-9-d_4 is also smoother, has higher symmetry, and is more extensively dispersed than the POMF of UiO-68-d_4 (*cf.* Figures 12a and 13a). In addition, the local motion is more symmetrical in the presence of the macrocycle, with $R_{\parallel}/R_{\perp}$ being 1.1×10^3 for UWDM-9-d_4 and 3.2×10^3 for UiO-68-d_4 (Table 3). Finally, the diffusion tilt, β_{MQ}, assumes the standard value of 64° (63° at the high temperature of 125 °C) in UWDM-9-d_4, in evidence of the straightforward local geometry, while it digresses from this value in UiO-68-d_4 (Tables 1 and 2).

The features delineated in the previous paragraph are not likely to be caused by limited free volume. They could be caused by cooperative phenyl-ring/macrocycle dynamics, stimulated by the high porosity and periodic crystalline nature of the MOFs studied. Independent phenyl-d_4 dynamics in the UiO-68-d_4 cavity is more elaborate; it suits optimally the character of the phenyl ring and its immediate surroundings. Cooperative phenyl-ring/macrocycle dynamics in the UWDM-9-d_4 cavity has a simpler potential; it suits reasonably well the character of both constituents and their surroundings, with the benefit of enhanced stability due to dynamic-structure uniformity.

It is of interest to also compare activation energies for local motion. Only three data points are available for every rate constant, the changes with varying temperature in $R_{\perp}$ are small, and $R_{\parallel}$ of UiO-68-d_4 is already in the extreme motional narrowing limit. Hence, only limited information is expected. Figure S3 of the Supporting Information shows the relevant Arrhenius plots that yield E_{act}(UiO-68-d_4, $R_{\perp}$) = 2.2 ± 0.01 kJ/mol, E_{act}(UWDM-9-d_4, $R_{\perp}$) = 2.1 ± 0.3 kJ/mol, and E_{act}(UWDM-9-d_4, $R_{\parallel}$) = 10.2 ± 0.5 kJ/mol. These values are comparable in magnitude to activation energies reported for the diffusive local motion of methyl groups in hydrated threefold symmetric Aβ_{40}-amyloid fibrils.[15] MSM analysis found that the phenyl-ring of UWDM-9-d_4 is wobbling around the quasi-C_2 symmetry axis with an activation energy of 27 ± 1 kJ/mol.[28] That motion differs substantially from diffusion.

3.5. MOMD and MSM Interpretations.

The pictures of structural dynamics of UiO-68-d_4 and UWDM-9-d_4 emerging from these two different analyses are summarized below.

3.5.1. MOMD. The key physical quantities include the local potential, u; the local diffusion tensor, $\boldsymbol{R}$; and the polar angle β_{MQ}. Together, they depict a clear physical picture. The forms of the potential, u, and the equilibrium probability distribution, $\exp(-u)$, provide information on the local structure and the spatial distribution of the probe, respectively. β_{MQ} = 64° (63° at the high temperature of 125 °C) obtained for UWDM-9-d_4 indicates that standard geometry (consistent with the notion of "conformational isomerism") prevails for this MOF. On the other hand, UiO-68-d_4 exhibits digressions from standard geometry on the order of several degrees. As expected, in the absence of structural changes, the diffusion rate constants, $R_{\parallel}$ and $R_{\perp}$, increase with increasing temperature. The values found for the order parameters, S_{xx}, S_{yy}, and S_{zz}, assign the main local ordering/local diffusion axis to the symmetry axis of the phenyl-d_4 rotor. For UiO-68-d_4, two local structural changes (in the sense of new features of the dynamic structure), occurring at −75 °C and approximately at 100 °C, are detected.

The local potential, u, is more complex in UiO-68-d_4 in comparison to that of UWDM-9-d_4, which is simpler (*i.e.*, smoother, broader, and more symmetrical). Furthermore, the $\boldsymbol{R}$ tensor is more symmetrical in UWDM-9-d_4. Finally, for UWDM-9-d_4, the local geometry is standard[33] (or nearly so). As pointed out above, simpler restricted motion is consistent with cooperative dynamics of the two mobile components in the UWDM-9-d_4 cavity.

3.5.2. MSM. Symmetry-related jumps of the phenyl-d_4 ring around the pseudo-C_2 axis, identified as the symmetry axis of the terphenyldicarboxylate linker, are considered. For UiO-68-d_4, a four-site exchange model is used, comprising three symmetry-related jumps. The rate constant k_1 refers to 90° jumps at one side of C_2; the rate constants k_2 and k_3 refer to 90 and 180° jumps across C_2, respectively. k_1 increases with increasing temperature; the intermediate rates $k_2 = 10^4$ and $k_3 = 10^3$ s^{-1} are temperature-invariant. The geometric relation between the quadrupolar tensor frame and C_2 is expressed in terms of the angles α, β, β', γ, and γ'. In MSM, the abrupt change in the ^{2}H spectrum of UiO-68-d_4 at −75 °C is

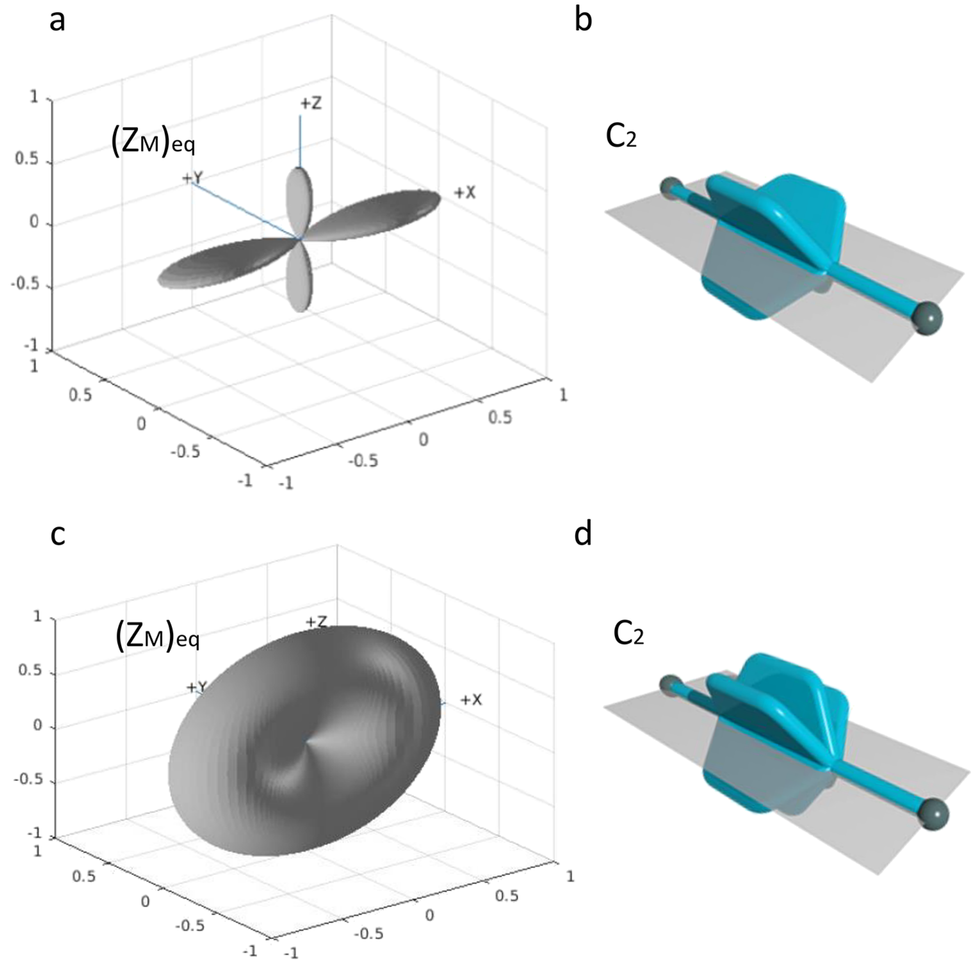

Figure 14. (a) Typical MOMD-derived orientational probability distribution, $P_{eq} = \exp(-u)$, of Z_M (fixed in the phenyl-d_4 ring) around $(Z_M)_{eq}$ (fixed in the director frame, C) for UiO-68-d_4. (b) Distribution of the four equilibrium phenyl-d_4 ring positions of UiO-68-d_4 around the pseudo-C_2 axis. (c) Typical MOMD-derived orientational probability distribution, $P_{eq} = \exp(-u)$, of Z_M (fixed in the phenyl-d_4 ring) around $(Z_M)_{eq}$ (fixed in the director frame, C) for UWDM-9-d_4. (d) Distribution of the six equilibrium phenyl-d_4 ring positions of UWDM-9-d_4 around the pseudo-C_2 axis.

attributed to a sudden onset of fast motion that is indicated by the narrower patterns, and no observation of clear intermediate motional regime signals. The abrupt change occurring at 100 °C (in the fast motion limit) is ascribed to k_1, k_2, and k_3 assuming their extreme narrowing limit values; the three jump angles becoming 84, 96, and 180° instead of the established set of 90, 90, and 180°; and the angles $\gamma\gamma'$ becoming ± 48, $\mp 48°$ instead of the established set of ± 45, $\mp 45°$. The unusual rounded-peak appearance of the UiO-68-d_4 spectra is not reproduced but rather is attributed to low intensity signals that may be indicative of some dynamical processes in the intermediate motional regime.

For UWDM-9-d_4, a six-site exchange model is used. There are two types of symmetry-related jumps: k_1 represents fast wobbling at one side of the pseudo-C_2 axis with $\gamma = 0$, $\gamma' = \pm 45°$ and a rate of 10^7 s^{-1}; k_2 represents 90° jumps across C_2 occurring with a rate of 10^4 s^{-1}. Both k_1 and k_2 are independent of temperature (over the range of observed spectra). A third static component is considered. The model consists of a weighted average superposition of the static component and the combined two dynamic components. The static component dominates the ^{2}H lineshape at lower temperatures, and the combined mobile components dominate it at higher temperatures.

Both the MOMD and MSM analyses find that the presence of the macrocycle in the MOF cavity has a substantial effect on the dynamics of the phenyl-d_4 ring. Both pictures of structural dynamics are complex. They comprise substantial information that provides snapshots of possible contributions to the big picture despite not converging into a unified description.

3.5.3. MOMD versus MSM. A limited comparison between these two approaches may be carried out given that $(Z_M)_{eq}$ in MOMD and the pseudo-C_2 axis in MSM are formally analogous and $(C-D)_{eq}$ is common to both methods.

Figure 14a is the same as Figure 12b, and Figure 14c is the same as Figure 13b. Around $(Z_M)_{eq}$, there is an ensemble of Z_M axes, each fixed (together with the respective C−D bond) in a given phenyl-d_4 ring (*cf.* Figure 3c). Z_M (hence, also C−D) is distributed in conformational space in accordance with the form of the local potentials depicted in Figures 12a and 13a. The analysis is consistent for the two MOFs studied.

Figure 14b,d features the pseudo-C_2 MSM axis that points in the same direction as $(Z_M)_{eq}$. The distribution of the probe in conformational space is given by four (six) equilibrium phenyl-d_4 ring positions for UiO-68-d_4 (UWDM-9-d_4) around the pseudo-C_2 axis, among which the phenyl-d_4 ring is exchanging. This is only a partial picture because additional motional modes contributing to the overall MSM models, which differ for the two MOFs considered, are not taken into consideration in MSM but are subsumed in the MOMD description. We do note that both approaches yield higher symmetry of the probe distribution for the MOF that comprises the mobile macrocycle (Figure 14c,d versus Figure 14a,b). This represents the extent to which MOMD and MSM may be compared.

4. CONCLUSIONS

We developed the MOMD approach for the analysis of ^{2}H NMR lineshapes in the solid state in terms of a collective motional mode consistent with the experimental resolution. Here we apply it to the UWDM-9-d_4 metal−organic framework (MOF) that is composed of a phenyl-d_4 rotor as probe and a mobile crown ether and to the UiO-68-d_4 MOF that is only composed of the phenyl-d_4 rotor. In the absence of the mobile macrocycle, the local potential at the C−D site, comprising four terms, is highly rhombic and relatively weak. The local C−D diffusion exhibits substantial axiality, and the local geometry digresses to some extent from the standard arrangement. Increasing the temperature results in faster diffusion and reduced strength and rhombicity of the potential. Two abrupt local structural changes are detected.

In the presence of the mobile macrocycle (UWDM-9-d_4 cavity), the C−D diffusion is slowed down and a two-term potential broader in shape and more symmetrical suffices. The local ordering (defined in terms of the corresponding local potential) is nearly axially symmetric, and the local geometry has a standard character. These features are consistent with cooperative motion of the two mobile components in the cavity of UWDM-9-d_4. This renders the dynamics simpler, promoting dynamic-structure uniformity and MOF/MIM stability.

A previous interpretation of the same experimental data based on the multi-simple-mode (MSM) reasoning is also discussed. The different MOMD-based and MSM-based perspectives of structural dynamics have been delineated above. While the two interpretations differ, the pseudo-C_2 axis in MSM may be considered to be the formal analogue of the equilibrium orientation of the main ordering/diffusion axis in MOMD.

One may conclude that MOMD serves as a tool for collectively monitoring motions involving several mobile components of MOFs. This should be helpful in designing MOF-based molecular machines.

■ ASSOCIATED CONTENT

Supporting Information

The Supporting Information is available free of charge at https://pubs.acs.org/doi/10.1021/acs.jpcb.1c10120.

> Experimental and calculated MOMD spectra of UiO-68-d_4 from Figure 9 aligned vertically with the inner and outer divergences marked; experimental and calculated MOMD spectra of UWDM-9-d_4 from Figure 11 aligned vertically with the inner and outer divergences marked; and Arrhenius plots for the parallel and perpendicular local diffusion rate constants of UWDM-9-d_4 and the perpendicular local diffusion rate constant of UiO-68-d_4 (PDF)

■ AUTHOR INFORMATION

Corresponding Authors

Eva Meirovitch − *The Mina and Everard Goodman Faculty of Life Sciences, Bar-Ilan University, Ramat-Gan 52900, Israel;* orcid.org/0000-0001-5117-5079; Phone: 972-3-531-8049; Email: eva.meirovitch@biu.ac.il

Jack H. Freed − *Baker Laboratory of Chemistry and Chemical Biology, Cornell University, Ithaca, New York 14853-1301, United States;* orcid.org/0000-0003-4288-2585; Phone: 607-255-3647; Email: jhf3@cornell.edu

Authors

Zhichun Liang − *Baker Laboratory of Chemistry and Chemical Biology, Cornell University, Ithaca, New York 14853-1301, United States*

Robert W. Schurko − *Department of Chemistry and Biochemistry, Florida State University, Tallahassee, Florida 32306, United States; National High Magnetic Field Laboratory, Tallahassee, Florida 32310, United States;* orcid.org/0000-0002-5093-400X

Stephen J. Loeb − *Department of Chemistry and Biochemistry, University of Windsor, Windsor, Ontario N9B 3P4, Canada;* orcid.org/0000-0002-8454-6443

Complete contact information is available at: https://pubs.acs.org/10.1021/acs.jpcb.1c10120

Notes

The authors declare no competing financial interest.

■ ACKNOWLEDGMENTS

This work was supported by the Israel−U.S.A. Binational Science Foundation (Grant No. 2016097 to E.M. and J.H.F.) and the Israel Science Foundation (Grant No. 288/20 to E.M.). This work was also supported by NIH/NIGMS grant P41GM103521 to J.H.F. R.W.S. is grateful for the research support from The Florida State University and the National High Magnetic Field Laboratory (NHMFL), which is funded by the National Science Foundation Cooperative Agreement (DMR-1644779) and by the State of Florida, as well as the support of the National Science Foundation Chemical Measurement and Imaging Program, with partial co-funding from the Solid State and Materials Chemistry Program (NSF-2003854). S.J.L. acknowledges the Natural Sciences and Engineering Research Council of Canada for support of a Discovery Grant (RGPIN-2018_101694) and a Canada Research Chair.

■ REFERENCES

(1) Spiess, H. W. *Dynamic NMR spectroscopy*, Diehl, P.; Fluck, E.; Kosfeld, R. Eds., 1978, Vol. *15*, pp. 55−241.

(2) Huang, T. H.; Skarjune, R. P.; Wittebort, R. J.; Griffin, R. G.; Oldfield, E. Restricted Rotational Isomerization in Polymethylene Chains. *J. Am. Chem. Soc.* **1980**, *102*, 7377−7379.

(3) Batchelder, L. S.; Sullivan, C. E.; Jelinski, L. W.; Torchia, D. A. Characterization of Leucine Side-Chain Reorientation in Collagen Fibrils by Solid-State ^{2}H NMR. *Proc. Natl. Acad. Sci. U. S. A.* **1982**, *79*, 386−389.

(4) Schurko, R. W.; Wi, S.; Frydman, L. Dynamic Effects on the Powder Line Shapes of Half-Integer Quadrupolar Nuclei: A Solid-State NMR Study of XO4- Groups. *J. Phys. Chem. A* **2002**, *106*, 51−62.

(5) Vold, R. L.; Hoatson, G. L. Effects of Jump Dynamics on Solid State Nuclear Magnetic Resonance Line Shapes and Spin Relaxation Times. *J. Magn. Reson., Ser. B* **2009**, *198*, 57−72.

(6) Echodu, D.; Goobes, G.; Shajani, Z.; Pederson, K.; Meints, G.; Varani, G.; Drobny, G. Furanose Dynamics in the *Hha*I Methyltransferase Target DNA Studied by Solution and Solid-State NMR Relaxation. *J. Phys. Chem. B* **2008**, *112*, 13934−13944.

(7) *Solid-State NMR Studies of Biopolymers*, Eds. McDermott, A. E.; Polenova, T. John Wiley and Sons, U.K., 2010.

(8) Krushelnitsky, A.; Reichert, D.; Saalwachter, K. Solid-State NMR Approaches to Internal Dynamics of Proteins: from Picoseconds to Microseconds and Seconds. *Acc. Chem. Res.* **2013**, *46*, 2028−2036.

(9) Meirovitch, E.; Liang, Z.; Freed, J. H. Protein Dynamics in the Solid State from ^{2}H NMR Line Shape Analysis: A Consistent Perspective. *J. Phys. Chem. B* **2015**, *119*, 2857−2868.

(10) Schanda, P.; Ernst, M. Studying Dynamics by Magic-Angle-Spinning Solid-State NMR Spectroscopy: Principles and Applications to Biomolecules. *Prog. Nucl. Magn. Reson. Spectrosc.* **2016**, *96*, 1−46.

(11) Au, D. F.; Ostrovski, D.; Fu, R.; Vugmeyster, L. Solid-State NMR Reveals a Comprehensive View of the Dynamics of the Flexible Disordered N-Terminal Domain of Amyloid-*β* Fibrils. *J. Biol. Chem.* **2019**, *294*, 5840−5853.

(12) Smith, A. A.; Ernst, M.; Meier, B. H.; Ferrage, F. Reducing Bias in the Analysis of Solution-State NMR Data with Dynamics Detectors. *J. Chem. Phys.* **2019**, *151*, 034102−034115.

(13) Meirovitch, E.; Nayeem, A.; Freed, J. H. Analysis of Protein-Lipid Interactions Based on Model Simulations of ESR Spectra. *J. Phys. Chem.* **1984**, *88*, 3454−3465.

(14) Meirovitch, E.; Liang, Z.; Freed, J. H. Protein Dynamics in the Solid State from ^{2}H NMR Lineshape Analysis. II MOMD Applied to C-D and C-CD$_3$ Probes. *J. Phys. Chem. B* **2015**, *119*, 14022−14032.

(15) Meirovitch, E.; Liang, Z.; Freed, J. H. MOMD Analysis of NMR Lineshapes from A*β*-Amyloid Fibrils: A New Tool for Characterizing Molecular Environments in Protein Aggregates. *J. Phys. Chem. B* **2018**, *122*, 4793−4801.

(16) Meirovitch, E.; Liang, Z.; Freed, J. H. Phenyl-Ring Dynamics in Amyloid Fibrils and Proteins: The Microscopic-Order-Macroscopic-Disorder Perspective. *J. Phys. Chem. B* **2018**, *122*, 8675−8684.

(17) Meirovitch, E.; Liang, Z.; Freed, J. H. Protein Dynamics in the Solid State from ^{2}H NMR Line Shape Analysis. III. MOMD in the Presence of Magic Angle Spinning. *Solid State Nucl. Magn. Reson.* **2018**, *89*, 35−44.

(18) Meirovitch, E.; Liang, Z.; Freed, J. H. Structural Dynamics by NMR in the Solid State: The Unified MOMD Perspective Applied to Organic Frameworks with Interlocked Molecules. *J. Phys. Chem. B* **2020**, *124*, 6225−6235.

(19) Polnaszek, C. F.; Bruno, G. V.; Freed, J. H. ESR Lineshapes in the Slow-Motional Region: Anisotropic Liquids. *J. Chem. Phys.* **1973**, *58*, 3185−3199.

(20) Polnaszek, C. F.; Freed, J. H. Electron Spin Resonance Studies of Anisotropic Ordering, Spin Relaxation, and Slow Tumbling in Liquid Crystalline Solvents. *J. Phys. Chem.* **1975**, *79*, 2283−2306.

(21) Lin, W. J.; Freed, J. H. Electron Spin Resonance Studies of Anisotropic Ordering, Spin Relaxation, and Slow Tumbling in Liquid Crystalline Solvents: 3 Smectics. *J. Phys. Chem.* **1979**, *83*, 379−401.

(22) Vukotic, V. N.; Harris, K. H.; Zhu, K.; Schurko, R. W.; Loeb, S. J. Metal-Organic Frameworks with Dynamic Interlocked Components. *Nat. Chem.* **2012**, *4*, 456−460.

(23) Zhu, K.; Vukotic, V. N.; O'Keefe, C. A.; Schurko, R. W.; Loeb, S. J. Metal-Organic Frameworks with Mechanically Interlocked Pillars: Controlling Ring Dynamics in the Solid-State via a Reversible Phase Transition. *J. Am. Chem. Soc.* **2014**, *136*, 7403−7409.

(24) Vukotic, V. N.; O'Keefe, C. A.; Zhu, K.; Harris, K. J.; To, C.; Schurko, R. W.; Loeb, S. J. Mechanically Interlocked Linkers inside Metal-Organic Frameworks: Effect of Ring Size on Rotational Dynamics. *J. Am. Chem. Soc.* **2015**, *137*, 9643−9651.

(25) Farahani, N.; Zhu, K.; O'Keefe, C. A.; Schurko, R. W.; Loeb, S. J. Thermally Driven Dynamics of a Rotaxane Wheel about an Imidazolium Axle inside a Metal-Organic Framework. *ChemPlusChem* **2016**, *81*, 836−841.

(26) Olson, M. A. Shuttling in the Solid State. *Nat. Chem.* **2015**, *7*, 470−471.

(27) Cavka, J. H.; Jakobsen, S.; Olsbye, U.; Guillou, N.; Lamberti, C.; Bordiga, S.; Lillerud, K. P. A New Zirconium Inorganic Building Brock Forming Metal Organic Framework with Exceptional Stability. *J. Am. Chem. Soc.* **2008**, *130*, 13850−13851.

(28) Wilson, B. H.; Vojvodin, C. S.; Gholami, G.; Abdulla, L. M.; O'Keefe, C. A.; Schurko, R. W.; Loeb, S. J. Precise Spatial Arrangement and Interaction between Two Different Mobile Components in a Metal-Organic Framework. *Chem* **2021**, *7*, 1−10.

(29) Tchaicheeyan, O.; Freed, J. H.; Meirovitch, E. Local Ordering at Mobile Sites in Proteins from Nuclear Magnetic Resonance Relaxation: The Role of Site Symmetry. *J. Phys. Chem. B* **2016**, *120*, 2886−2898.

(30) Polimeno, A.; Freed, J. H. A Many-Body Stochastic Approach to Rotational Motions in Liquids, *Advances in Chemical Physics LXXXIII*, Prigogine, I; Rice, S. A. Eds. (Wiley, NY 1993), 89−204.

(31) Schneider, D. J.; Freed, J. H. *Calculating Slow Motional Magnetic Resonance Spectra: A User Guide. In Biological Magnetic Resonance*, Plenum, New York 1989, Vol. *8*, pp. 1−76, DOI: 10.1007/978-1-4613-0743-3_1.

(32) Barnes, J. P.; Freed, J. H. Dynamics and Ordering in Mixed Model Membranes of Dimyristoylphosphatidylcholine and Dimyristoylphosphatidylserine: A 250 GHz Electron Spin Resonance Study Using Cholestane. *Biophys. J.* **1998**, *75*, 2532−2546.

(33) Schadt, R. J.; Cain, E. J.; English, A. D. Simulation of One-Dimensional NMR Line Shapes. *J. Phys. Chem.* **1993**, *97*, 8387−8392.

(34) Gonzales-Nelson, A.; Coudert, F.-X.; van der Veen, M. A. Rotational Dynamics of Linkers in Metal-Organic Frameworks. *Nanomaterials* **2019**, *9*, 330.